Steel and Composite Structures, *Vol. 33, No. 6* (*2019*) *777-792*
DOI: https://doi.org/10.12989/scs.2019.33.6.777

Rapid S-N type life estimation for low cycle fatigue of high-strength steels at a low ambient temperature

Liuyang Feng [a] and Xudong Qian*

Department of Civil and Environmental Engineering, *Centre for Offshore Research and Engineering*, *National University of Singapore*, *Singapore 117576*

(*Received March 23, 2019, Revised November 21, 2019, Accepted November 30, 2019*)

Abstract. This paper presents a new efficient approach to estimate the S-N type fatigue life assessment curve for S550 high strength steels under low-cycle actions at –60°C. The proposed approach combines a single set of monotonic tension test and one set of fatigue tests to determine the key material damage parameters in the continuum damage mechanics framework. The experimental program in this study examines both the material response under low-cycle actions. The microstructural mechanisms revealed by the Scanning Electron Microscopy (SEM) at the low temperature, furthermore, characterizes the effect due to different strain ratios and low temperature on the low-cycle fatigue life of S550 steels. Anchored on the experimental results, this study validates the S-N curve determined from the proposed approach. The S-N type curve determined from one set of fatigue tests and one set of monotonic tension tests estimates the fatigue life of all specimens under different strain ratios satisfactorily.

Keywords: low-cycle fatigue; low temperature; continuum damage mechanics; cyclic material property; mean stress relaxation

1. Introduction

The increasing activities by various industries in the Arctic stimulate research studies on the mechanical capability of the high-strength steel at low temperatures which represents a common engineering material for Arctic infrastructures. Fatigue issues caused by the ice-induced vibration, wave and wind have emerged as a critical concern for the Arctic structures. Over the last few decades, most experimental fatigue investigations focus on the high-cycle fatigue problems at low temperatures (Kawasaki *et al*. 1975, Liao *et al*. 2018, Walters *et al*. 2016), and the low and high-cycle fatigue assessment of large-scale engineering structures (Zhao *et al*. 2018, Wang *et al*. 2013, Ju *et al*. 2018, Liu *et al*. 2017, Lim *et al*. 2013, Ertas and Yilmaz 2014, Ghazijahani *et al*. 2015, Sakr *et al*. 2019, Maalek *et al*. 2019). The research efforts on the low-cycle fatigue of high-strength steels at a low temperature remain limited. Botshekan *et al*. (1998) compared the low-cycle fatigue properties of AISI 316LN steel. Shibata *et al*. (1985) investigated the cyclic softening and hardening properties of austenitic steels at low temperatures. Previous experimental findings also revealed a significant effect of the load ratios on the measured fatigue life under low-cycle actions (Arcari *et al*. 2009, Branco *et al*. 2012, Paul *et al*. 2015). In addition, the cumulative irrecoverable plastic strain forces the mean stress to decrease gradually to zero, creating a phenomenon known as the Mean Stress Relaxation (MSR) (Koh and Stephens 1991, Kourousis and Dafalias 2013, Gróza and Váradi 2017). The MSR behavior further complicates the effect caused by the non-zero mean stress on the low-cycle fatigue life at the low temperature. Therefore, research on low-cycle fatigue under different strain ratios is indispensable to develop a reliable approach for the low-cycle fatigue assessment at a low ambient temperature.

Engineering practices (Hobbacher 2016, Veritas 2010, ABS 2014) often follow the S-N curves to assess the fatigue life of structural components under different loadings. Different fatigue indicators (S) based on the stress, strain, and strain energy density have emerged in recent decades (Macha and Sosino 1999, Malagi and Danawade 2015, Maachou *et al*. 2016, Feng and Qian 2017, 2018). The conventional approach to determine the S-N curve is through a regression analysis in the logarithmic scale based on sufficient numbers of fatigue test results (ASTM E606/E606M 2012), rendering a power-law type relationship between the fatigue indicator and the total fatigue life. The power-type relationship is a highly-nonlinear equation, which often provides a good coefficient of determination for most of the above fatigue indicators, and therefore, tends to place a low emphasis on detailed physical interpretations of the material (Aeran *et al*. 2017). The selection of an appropriate fatigue life estimation approach requires a detailed understanding on the physical material response under cyclic actions. In addition, preparing for the large number of fatigue tests is often time-consuming and costly, particularly for the fatigue test under a low temperature. To alleviate the required number of fatigue specimens, some research works (Zhang *et al*. 2013,

*Corresponding author, Associate Professor,
E-mail: qianxudong@nus.edu.sg
[a] Ph.D., E-mail: fengliuyang@u.nus.edu

http://www.techno-press.org/?journal=scs&subpage=6
ISSN: 1229-9367 (Print), 1598-6233 (Online)

Amiri and Khonsari 2010) utilized the thermographic method for quick prediction of the fatigue life. However, the thermographic approach relies heavily on the accuracy of the temperature measurement system. The temperature evolution of the specimen in the fatigue test tends to be interfered by the heat convection and emissivity in the ambient environment. For engineering applications, such an approach requires a detailed monitoring of both the specimen temperature and the ambient temperature. Hence, a high-precision measurement system is essential for reliable and repeatable results. The Continuum Damage Mechanics (CDM) represents another efficient tool to estimate the fatigue damage growth based on a phenomenological description of the nucleation, growth and coalescence of microvoids (Bonora and Newaz 1998, Lemaitre 2012, Perera *et al*. 2001, Huang *et al*. 2014), and therefore, can provide a physical S-N relationship. The damage parameter quantifies the variation in the density, elastic modulus, micro-hardness, cyclic stress amplitude or electrical resistance. Chaboche and Lesne (1998) have initially developed a nonlinear continuous fatigue damage model to describe the deterioration in various phases including the microcrack-initiation and the microcrack-propagation, which has been further improved by researchers for different loading conditions and nonlinear damage accumulation (Shang and Yao 1999, Huang *et al*. 2014). Darveaux (2002) and Lau *et al*. (2002) proposed a damage initiation and evolution law based on the accumulated inelastic hysteresis strain energy per cycle. Ye and Wang (2001) have argued that the exhaustion in the static toughness of fatigued specimens reflects the inherent damage caused by the fatigue actions. They have proposed a fatigue damage evolution model based on the static toughness of the fatigued specimens. Lemaitre (2012) has integrated a constitutive equation with the damage state variable through the thermodynamic state potential, which is widely used for both monotonic and low-cycle fatigue ductile failure. The temperature-dependent damage parameters, insensitive to the loading types by the Lemaitre's damage model (Lemaitre 2012), provide a promising foundation to determine these damage parameters in the S-N relationship by using the monotonic tensile test. However, the S-N curve proposed by Lemaitre (2012) entails the following assumptions: (1) damage initiates at a constant critical cumulative plastic strain, and (2) the material is perfectly plastic.

The S550 high-strength steel investigated in this paper has the advantage of high strength to weight ratios, good weldability, improved toughness and good ductility, and has found wide applications in ships, marine and offshore structures and bridges. This paper reports the strain-controlled low-cycle fatigue experiments of S550 high-strength steel under different strain ratios at –60°C. Based on the experimental results, this study discusses the effects due to the non-zero strain ratios and the low temperature on the low-cycle fatigue life of S550 steel. To alleviate the large number of fatigue tests required to regress an S-N curve, this study proposes a new damage initiation criterion based on the experimental results. Under the framework of continuum damage mechanics, this study proposes a new hybrid approach, based solely on one set of monotonic tensile tests and one set of fatigue tests, to rapidly determine the S-N relationship for low-cycle fatigue.

2. Material and experimental details

Table 1 lists the chemical composition for the S550 steel studied in this paper. The experimental scheme focuses on the flat coupon specimens with 22 mm thickness and 400 mm length (Fig. 1(a)) under low-cycle fatigue loadings. The experimental procedure follows the ASTM E606/E606M (2012) in a low temperature chamber, as shown in Fig. 1(b). This study utilizes the liquid nitrogen to control the temperature in the chamber at a stable value of –60°C with a fluctuation within ±2°C through the J thermocouple. A calibrated extensometer with 50 mm gauge length monitors the nominal strain during the low-cycle fatigue test at the low temperature. The dynamic oscilloscope DL850 captures and stores 200~500 experimental data per second.

The experimental program includes 36 specimens under low-cycle loadings with four strain amplitudes ranging from

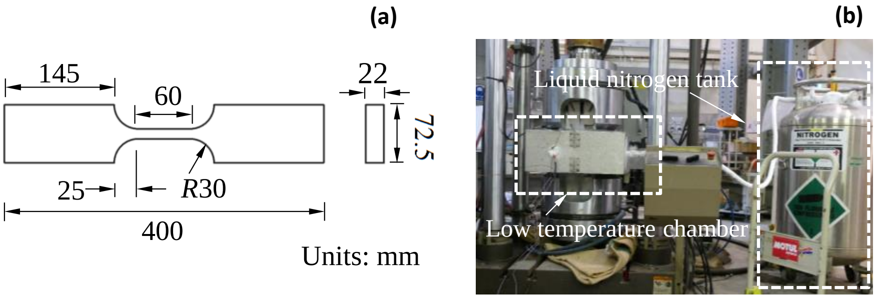

Fig. 1 (a) Geometrical dimensions of the flat coupon specimen; and (b) experimental set up

Table 1 Weight percentage for chemical compositions of S550 high strength steel

S550	Fe	C	Si	Mn	P	S	Cu	Cr	Ni	Mo
Weight (%)	96.19	0.106	0.327	1.41	0.010	0.002	0.121	0.454	0.918	0.462

0.5% to 1.25%, which correspond to the low-cycle fatigue regime. The strain ratio R_ε investigated in this paper covers three values: –1, 0.1 and 0.5. Each strain amplitude and strain ratio include three duplicated specimens. This study adopts a loading frequency ranging from 0.2 Hz to 0.5 Hz for the low-cycle fatigue test for stabilizing a slow constant strain changing rate. Each of the fatigue specimens experience a constant strain amplitude during the test. The post-test scanning electron microscopy (SEM) examines the microstructural features on the fatigue failure surface.

3. Experimental results

3.1 Low-cycle material properties

The hysteresis loops at half of the fatigue life under different strain amplitudes characterize the cyclic material property (Lefebvre and Ellyin 1984)

$$\varepsilon_a = \frac{\sigma_a}{E} + \left(\frac{\sigma_a}{K}\right)^{\frac{1}{n}} \tag{1}$$

where ε_a refers to the total strain amplitude, σ_a defines the stress amplitude at half of the fatigue life, E represents the elastic modulus, K denotes the cyclic strain hardening coefficient and n is the cyclic strain hardening exponent.

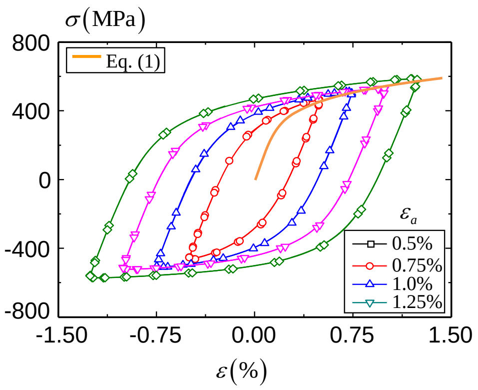

Fig. 2 The saturated hysteresis loops for four different strain amplitudes and cyclic stress-strain curve

Fig. 2 presents the hysteresis loops at half of the fatigue life under four strain amplitudes and the calibrated cyclic stress-strain curve of S550 with $E = 213$ GPa, $K = 1352$ MPa and $n = 0.18$ at –60°C.

Fig. 3(a) presents a similar trend in the variation of the normalized stress amplitudes with the normalized fatigue cycles under four different strain amplitudes. Cyclic softening exists under all four strain amplitudes, which is measured by a cyclic softening ratio $\tilde{S}$ in this study,

$$\tilde{S} = \frac{\sigma_a^{N=1} - \sigma_a^{N=0.5N_f}}{\sigma_a^{N=1}} \tag{2}$$

where $\sigma_a^{N=1}$ and $\sigma_a^{N=0.5N_f}$ define the stress amplitude at the first cycle and half of the fatigue life, respectively. As shown in Fig. 3(b), the cyclic softening ratios remain independent of the strain amplitudes at –60°C, similar to that at the room temperature (Feng and Qian 2018).

3.2 Non-Masing type behavior of S550

The Masing cyclic stress-strain curve defines the skeleton of the stabilized stress-strain curve, indicating the coincidence of the loading or unloading branch of the hysteresis curve under different strain amplitudes. In contrast, the non-Masing type behavior requires a master curve to evaluate the branch of the hysteresis loop at stabilized cycles (Lefebvre and Ellyin 1984). For S550 steel in this paper, the loading branch curve of the hysteresis loop at half of the fatigue life does not completely coincide with each other after shifting the tips of the loops to the origin, as shown in Fig. 4(a). Therefore, this study plots a master curve which is initially proposed by Ellyin (1989) by overlapping the loading branches of the hysteresis loop at half of the fatigue life under four strain amplitudes. The expression of the master curve in the auxiliary coordinate system, of which the origin locates at the lower tip of the hysteresis cycle under the smallest strain amplitude, reads

$$\Delta\varepsilon^* = \frac{\Delta\sigma^*}{E} + 2\left(\frac{\Delta\sigma^*}{2K^*}\right)^{\frac{1}{n^*}} \tag{3}$$

where n^* represents the hardening exponent and K^*

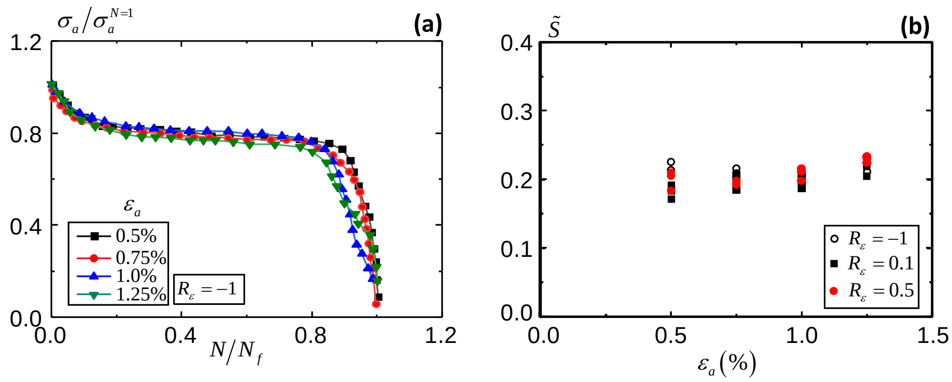

Fig. 3 (a) Variation of the normalized stress amplitude; under four strain amplitudes with increasing cycles; and (b) the cyclic softening ratio

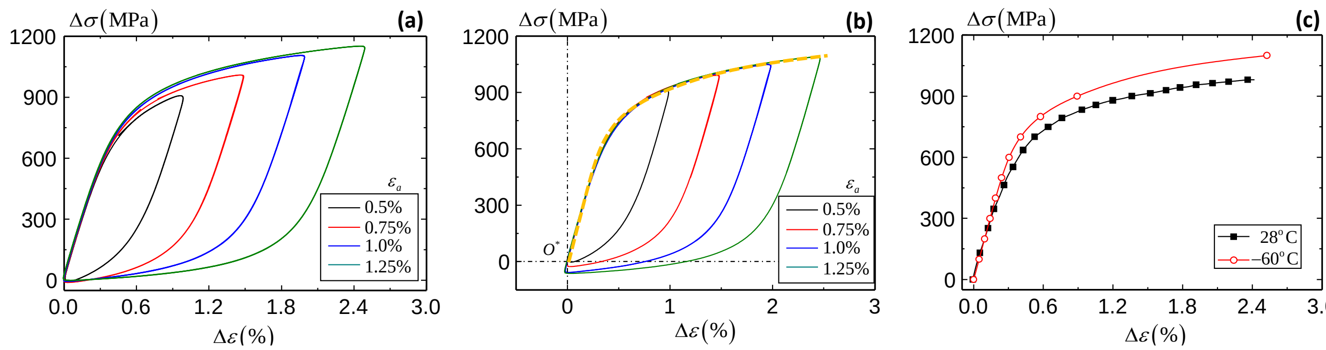

Fig. 4 (a) Non-Masing behavior of S550 steel; (b) master curve of non-Masing behavior for S550 steel; (c) comparison of the master curves at 28°C and –60°C

denotes the cyclic coefficient of the master curve in the auxiliary coordinate system. The increase in the proportional stress caused by the non-Masing type behavior is

$$\delta\sigma_o = \Delta\sigma - \Delta\sigma^* = \Delta\sigma - 2K^*\left(\frac{\Delta\varepsilon^{pl}}{2}\right)^{n^*} \tag{4}$$

Fig. 4(b) shows the master curve of S550 with E = 213 GPa, K^* = 1037 MPa, n^* = 0.138 and $\delta\sigma_o$ = 65.1 MPa. Fig. 4(c) compares the master curve of the S550 high-strength steel at the room temperature (Feng and Qian 2018) and that at –60°C.

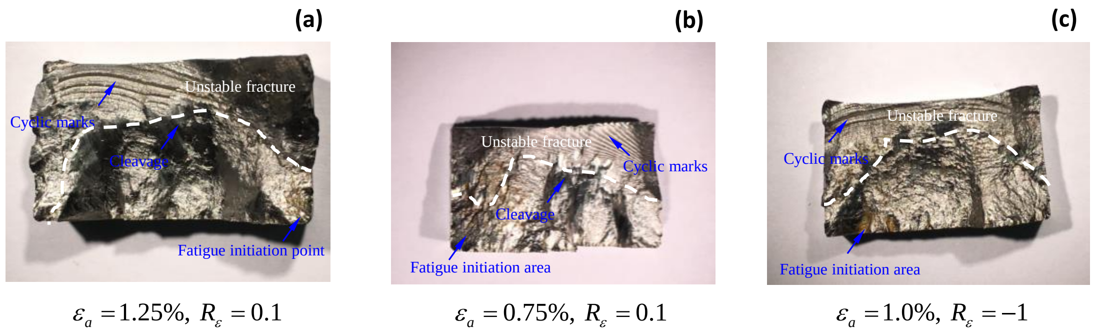

Fig. 5 Representative low-cycle fatigue failure surfaces under different strain amplitudes and ratios

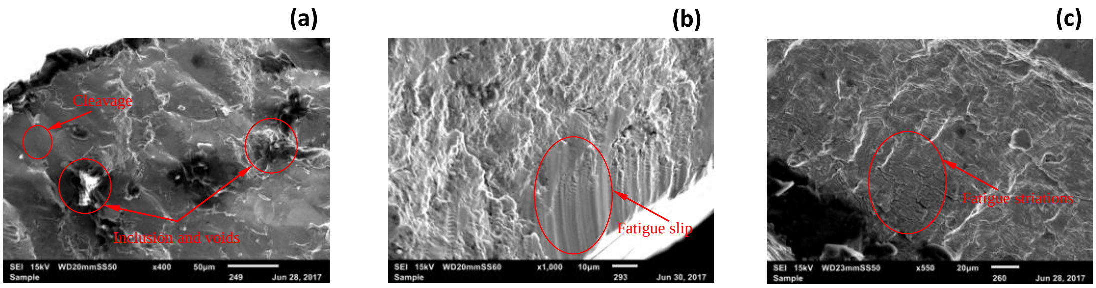

Fig. 6 Representative SEM micrographs of the crack initiation point under different magnification factors

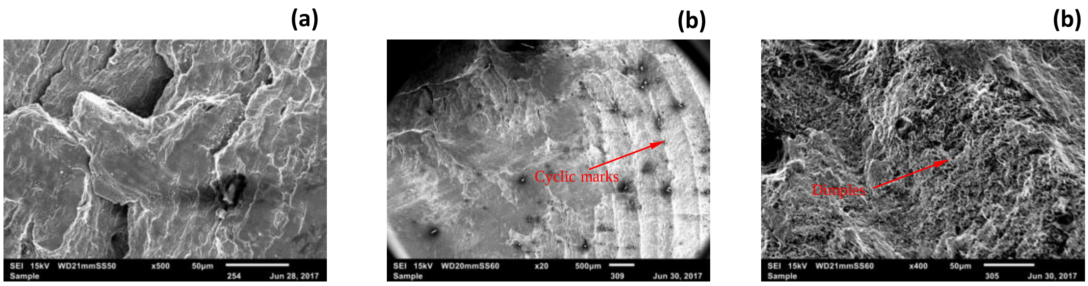

Fig. 7 Representative SEM micrographs of: (a) crack growth zone; and (b)-(c) final fracture zone

3.3 Fractography of the failure surface

Fig. 5 presents the representative macroscopic fatigue failure surfaces captured by a high-magnification camera. The typical fatigue process consists of three stages: the crack initiation, the crack growth and the final unstable fracture failure. Under the low temperature, the converging radial lines signify the crack initiation point near the surfaces of the flat specimens. There are clear fatigue crack striations and cleavage facets in the crack propagation zone. Macroscopic fatigue marks emerge in the final fracture zone.

Fig. 6 displays representative SEM micrographs of the crack initiation zone with different magnification factors. The larger inelastic deformation, intrusion/extrusion and corrosion near the surface lead to the initiation of the crack. In the crack initiation zone, some internal discontinuities (inclusions and voids in Fig. 6(a)), the fatigue slip bands (Fig. 6(b)), cleavage facets (Fig. 6(a)) and multiple small fatigue crack striations (Fig. 6(c)) are visible under the SEM.

Fig. 7(a) shows the representative SEM micrographs of the fatigue crack growth zone at –60°C. In contrast to the predominant crack striations in the fatigue crack growth zone at the room temperature (Feng and Qian 2018), cleavage fracture surfaces emerge in the crack growth zone at –60°C. Previous experimental investigations on S550 and other high-strength steels reveal a reduced fracture toughness at low ambient temperature (Chen *et al.* 2016, Zhang and Qian 2016). This increases the probability of cleavage failure at a low ambient temperature. Fig. 7(b) shows clear fatigue marks in the final fracture surface. Cleavage failure between the clear marks are observable in Fig. 7(b). Intense voids and dimples (Fig. 7(c)) under higher magnification factors imply the overload failure during the final failure process.

3.4 Mean stress relaxation

Non-fully reversed, strain-controlled fatigue tests usually produce a non-zero mean stress. The tensile mean stress generally facilitates the crack opening, and thus shortens the fatigue life, while the compressive mean stress prolongs the fatigue life (Koh and Stephens 1991). Meanwhile, as the plastic strain accumulates, the tensile/compressive mean stress approaches gradually to zero during the fatigue process (Lee *et al.* 2014). Fig. 8 depicts the variation of peak, valley and mean stresses with increasing fatigue cycles under four strain amplitudes with the strain ratios of 0.1 and 0.5. The mean stress reaches gradually zero prior to 10% of the total fatigue life for all strain amplitudes.

3.5 Effect of the strain ratios

Table 2 lists the total low-cycle fatigue life of the coupon specimens under different strain amplitudes with three different strain ratios. Due to the rapid mean stress relaxation, the fatigue life under different strain ratios thus does not display significant differences, particularly for the large strain amplitude, as shown in Fig. 9(a).

Superior to the stress or strain-based method, the energy-based approach incorporates the stress and strain in the deformation process. This study adopts the energy indicator ($\sigma_a^{N=1}\varepsilon_a$) previously proposed by Feng and Qian (2018) for the low-cycle fatigue results under the low temperature. The relationship between the fatigue life with the previously proposed fatigue energy indicator follows

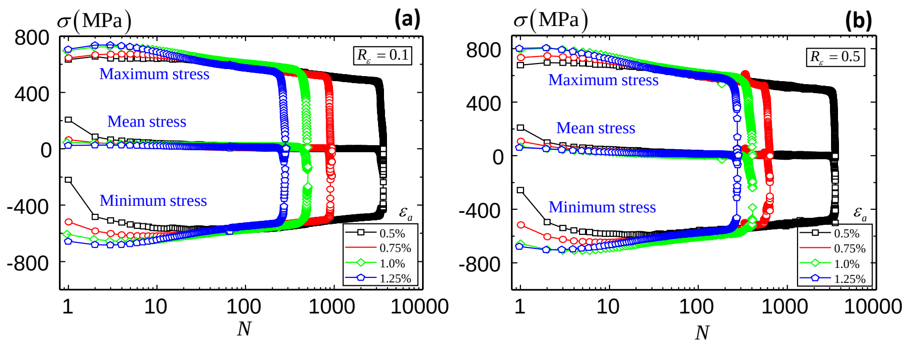

Fig. 8 Variation of the peak stress, valley stress and mean stress with increasing numbers of fatigue cycles under four strain amplitudes with strain ratios of: (a) 0.1; and (b) 0.5

Table 2 Total fatigue life of tests under different strain amplitudes

ε_a	$R_\varepsilon = -1$			$R_\varepsilon = 0.1$			$R_\varepsilon = 0.5$		
	Cycles to failure			Cycles to failure			Cycles to failure		
0.5%	3710	3514	-	4279	3958	3584	3462	3851	6347
0.75%	839	1186	1178	963	938	897	1020	667	838
1.0%	655	431	503	493	497	484	406	615	451
1.25%	294	325	339	269	293	241	265	287	255

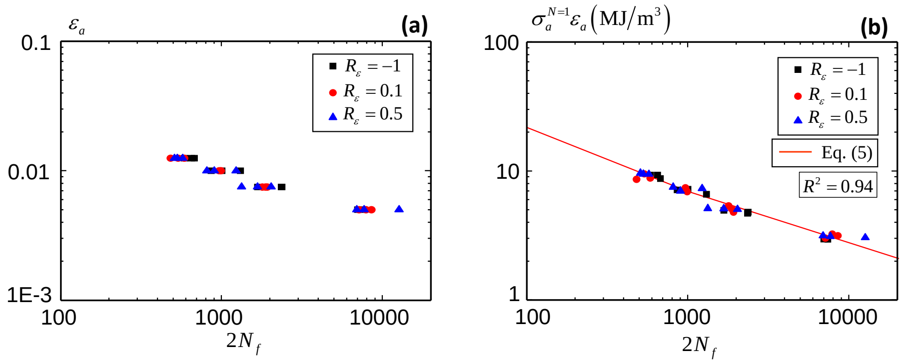

Fig. 9 Fatigue data assessment based on: (a) strain amplitude; and (b) energy indicator ($\sigma_a^{N=1}\varepsilon_a$)

Table 3 Values of parameters in Eq. (5) for S550 high strength steel at the low temperature

A_1 (MPa)	B_1	G_1 (MPa)	F_1
35.4	-0.301	357	-0.715

$$\sigma_a^{N=1}\varepsilon_a = A_1\left(2N_f\right)^{B_1} + G_1\left(2N_f\right)^{F_1} \tag{5}$$

Table 3 shows the parameters in Eq. (5), obtained through the least square error regression analysis. Fig. 9(b) plots the energy indicator ($\sigma_a^{N=1}\varepsilon_a$) with the number of load reversals to failure ($2N_f$). The coefficient of determination R^2 of 0.94 demonstrates the accuracy of the energy based on the fatigue indicator proposed by Feng and Qian (2018) at –60°C.

3.6 Effect of the low temperature

This section investigates the low temperature's effect on the fatigue life and examines the capability of the energy indicator ($\sigma_a^{N=1}\varepsilon_a$) in integrating the temperature effect.

Figs. 10(a)-(c) compare the fatigue life based on the strain amplitude at 28°C and –60°C with the strain ratios of –1, 0.1 and 0.5, respectively. For $R_\varepsilon = -1$, the difference in the fatigue lives at 28°C and –60°C is negligible. However, with R_ε of 0.1 and 0.5, the fatigue life at –60°C is smaller than that at 28°C, especially for larger strain amplitudes (1.0% and 1.25%). Fig. 10(d) shows all the low-cycle fatigue test data at two different temperatures based on the strain amplitude.

To elucidate the above phenomenon, Fig. 11 compares the hysteresis cycle at half of the fatigue life at 28°C and –60°C for the strain amplitude of 1.25% with R_ε of –1, 0.1

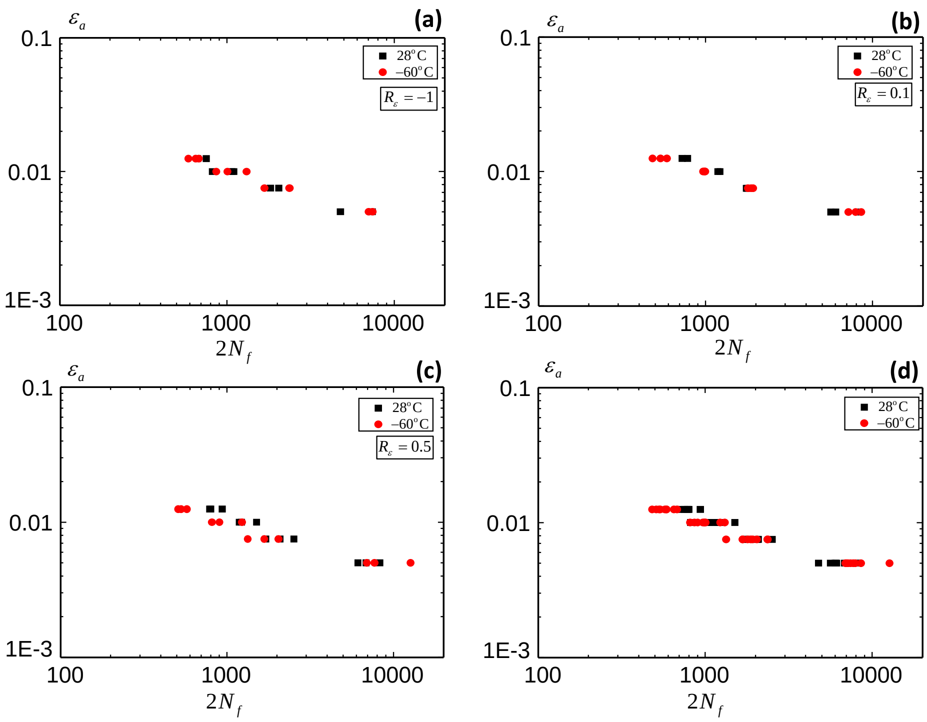

Fig. 10 Fatigue data at 28°C and –60°C with R_ε: (a) –1; (b) 0.1; (c) 0.5; and (d) all strain ratios

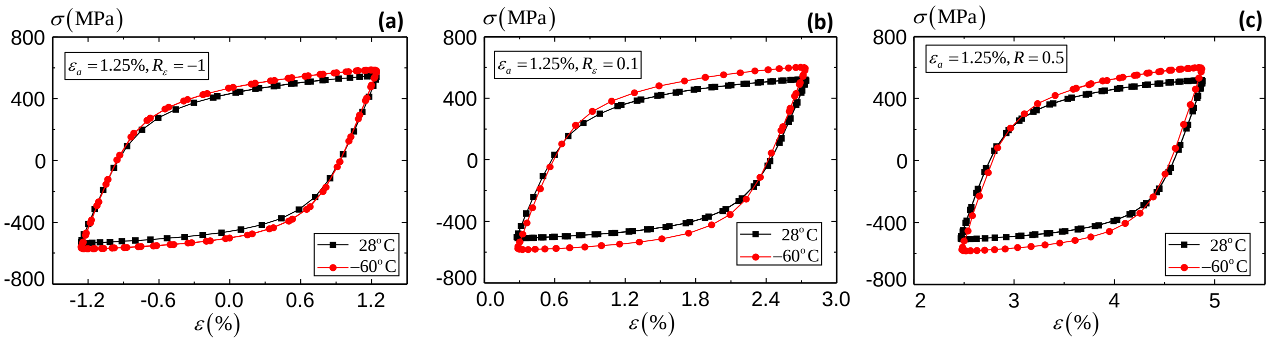

Fig. 11 Hysteresis loops at half of the fatigue life under 1.25% strain amplitude and strain ratios of: (a) –1; (b) 0.1; and (c) 0.5

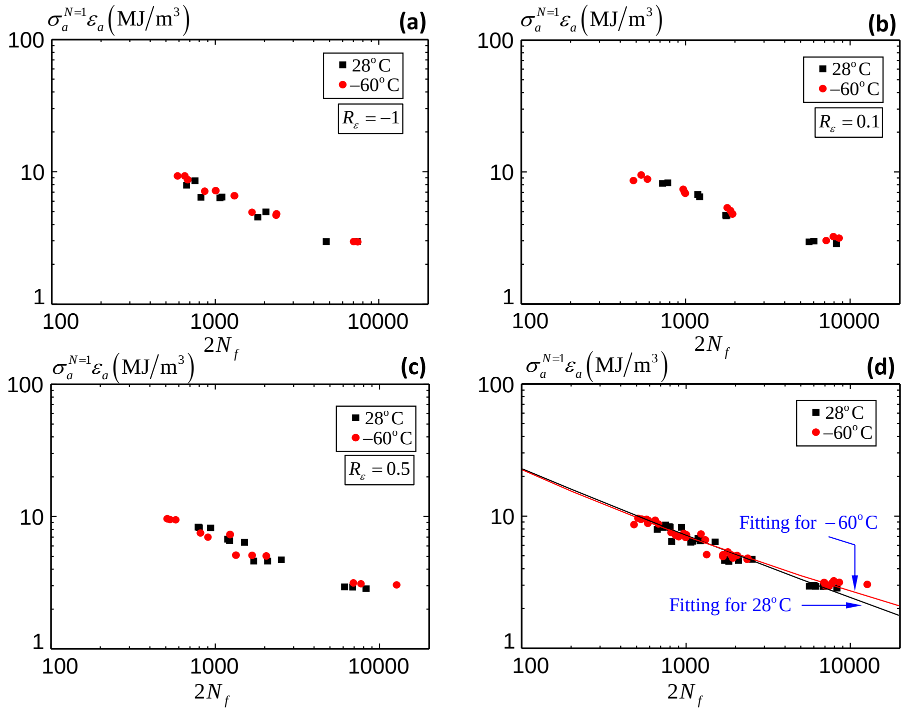

Fig. 12 Fatigue test data assessment using the energy indicator ($\sigma_a^{N=1}\varepsilon_a$) at 28°C and –60°C with R_ε: (a) –1; (b) 0.1; (c) 0.5; and (d) all strain ratios

and 0.5. As illustrated in Fig. 11, under the same strain amplitude, the area enveloped by the hysteresis loop under different temperatures is not always the same. For the R_ε of 0.1 and 0.5, the dissipated hysteresis energy at –60°C is larger than that at 28°C, therefore causes a shorter fatigue life. For the strain ratio of –1, the hysteresis loop area is approximately the same for 28°C and –60°C. Therefore, the difference between the fatigue lives measured at two different temperatures is negligible for $R_\varepsilon = -1$. In view of the different energy levels enveloped by the hysteresis loops at different temperatures in Fig. 11, the energy indicator ($\sigma_a^{N=1}\varepsilon_a$) provides an enhanced fatigue indicator, which is able to quantify the fatigue driving energy at different temperatures. Figs. 12(a)-(c) compare the fatigue test data based on the proposed energy indicator ($\sigma_a^{N=1}\varepsilon_a$) with R_ε of –1, 0.1 and 0.5, respectively. In contrast to the strain-based assessment in Fig. 10, the energy indicator ($\sigma_a^{N=1}\varepsilon_a$) integrates the temperature effect in the fatigue driving force and all the fatigue data under different temperature follows a uniform $\sigma_a^{N=1}\varepsilon_a$ - N curve. Fig. 12(d) presents all the fatigue test data based on the proposed energy indicator ($\sigma_a^{N=1}\varepsilon_a$) at 28°C and –60°C. The effect of the low temperature on the low-cycle fatigue life of S550 is negligible when assessed using the energy indicator ($\sigma_a^{N=1}\varepsilon_a$). The comparison of the best fitting line at 28°C and –60°C also verifies the accuracy of the energy indicator ($\sigma_a^{N=1}\varepsilon_a$) in capturing the temperature effect under low-cycle actions. However, the difference under a high-cycle action still exists, which requires more experimental efforts for an enhanced understanding.

4. Continuum damage mechanics

The continuum damage mechanics provides a physical interpretation of the material deterioration under external loadings. The fatigue indicator in the S-N curve derived from the CDM therefore yields an internal microstructural fatigue driving force. In contrast to the conventional approach in determining the S-N curve through dozens of low-cycle fatigue data, which is time-consuming, costly and discrete, the monotonic tensile test represents a more convenient approach to correlate the material damage with the applied loading (Ye and Wang 2001). To mitigate the time-consuming experiments for a large number of fatigue specimens, this section first introduces the theoretical framework of the thermodynamics-based continuum damage mechanics (Lemaitre 2012, Lemaitre and Desmorat 2005) and calibrates the cyclic elastic-plastic parameters following the procedure implemented in ABAQUS (2014). Thereafter, this study proposes a new damage initiation criterion and develops a hybrid approach to determine the S-N curve based only on one set of fatigue test and one set of monotonic tensile test, considering the cyclic elastic-plastic material properties.

4.1 Framework of CDM

Lemaitre (2012) associates the damage variable with the constitutive elastic-plastic relationship, which reflects the degradation in the material stiffness due to the nucleation, growth and coalescence of microstructural voids. The microstructural damage variable represents the reduction of the effective net area in a Representative Volume Element (RVE). For numerical implementation, the damage variable D describes the reduction in the material stiffness

$$\tilde{\sigma} = \frac{\sigma_0}{1-D} \tag{6}$$

where $\tilde{\sigma}$ denotes the effective stress in the damaged material and σ_0 represents the nominal stress. Under the strain equivalence principle, Eq. (6) becomes

$$\tilde{E} = E(1-D) \tag{7}$$

where $\tilde{E}$ represents the effective Young's modulus and E refers to the Young's modulus of the intact material. Therefore, the elastic strain and stress relationship follows

$$\varepsilon_{ij}^{e} = \frac{1+\nu}{E}\frac{\sigma_{ij}}{1-D} - \frac{\nu}{E}\frac{\sigma_{kk}}{1-D}\delta_{ij} \tag{8}$$

where ν is Poisson' ratio, ε_{ij}^{e} is the elastic strain tensor and δ_{ij} denotes the Kronecker delta.

To fulfil the second principle of thermodynamics, Lemaitre (2012) proposed a potential of dissipation function F, consisting of three terms (the plastic criterion function f, the nonlinear kinematic hardening term F_x and the damage potential F_D)

$$F = f + F_X + F_D \tag{9}$$

and the constitutive plastic evolution laws follow

$$\dot{\varepsilon}_{ij}^{P} = \dot{\lambda}\frac{\partial F}{\partial \sigma_{ij}}, \quad \dot{r} = -\dot{\lambda}\frac{\partial F}{\partial R}, \quad \dot{\alpha}_{ij} = -\dot{\lambda}\frac{\partial F}{\partial X_{ij}} \tag{10}$$

where $\dot{\lambda}$ is the multiple factor, ε_{ij}^{p} represents the plastic strain tensor, R and X_{ij} denote the isotropic hardening stress and the kinematic backstress tensor, respectively.

The kinematic law of damage evolution reads

$$\dot{D}_{ij} = \dot{\lambda}\frac{\partial F}{\partial Y} = \frac{\partial F_D}{\partial Y}\dot{\lambda} \tag{11}$$

where Y is the strain energy density release rate and follows

$$Y = \frac{\sigma_{eq}^2}{2E(1-D)^2}\left[\frac{2}{3}(1+\nu) + 3(1-2\nu)\left(\frac{\sigma_H}{\sigma_{eq}}\right)^2\right] \tag{12}$$

where σ_{eq} represents the equivalent stress, σ_H is the hydrostatic stress and σ_H/σ_{eq} denotes the stress triaxiality ratio.

A more accurate expression of the potential of dissipation F follows,

(1) For the plastic criterion function

$$f = \left(\frac{\sigma}{1-D} - X\right)_{eq} - R - \sigma_y \tag{13}$$

where X and R are the kinematic backstress and isotropic hardening stress, σ_y denotes the initial yield strength, and

$$\left(\frac{\sigma}{1-D} - X\right)_{eq} = \sqrt{\frac{3}{2}\left(\frac{\sigma_{ij}^{'}}{1-D} - X_{ij}^{'}\right)\left(\frac{\sigma_{ij}^{'}}{1-D} - X_{ij}^{'}\right)} \tag{14}$$

where σ_{ij}' and X_{ij}' are deviatoric stress and back stress tensors.

(2) For the nonlinear kinematic hardening term

$$F_X = \frac{3\gamma}{4C}X_{ij}^{'}X_{ij}^{'} \tag{15}$$

where C and γ denote the initial kinematic hardening modulus and the rate at which the kinematic hardening modulus decreases with increasing plastic deformation, respectively.

(3) For the damage potential function

$$F_D = \frac{S}{(1+s)(1-D)}\left(\frac{Y}{S}\right)^{1+s} \tag{16}$$

where S and s are the corresponding material damage parameters. The damage potential derives from the microscopic nucleation, growth and coalescence of microcavities by large local plastic deformation, applicable for ductile isotropic damage evolutions including the low-cycle fatigue and monotonic tensile test. The S and s thus depend solely on the temperature.

4.2 Plastic material properties

To determine the plastic kinematic and isotropic hardening parameters, this study adopts the constitutive material formulation originally proposed by Frederick and

Armstrong (1966) and subsequently modified by Chaboche (1986, 1989). The isotropic hardening relationship defines the size evolution of the yield surface while the nonlinear kinematic law describes the translation of the center of the yield surface without changing the size of the yield surface. The kinematic and isotropic hardening properties depend on the effective, cumulative plastic strain p, defined by its rate

$$\dot{p} = \left(\frac{2}{3}\dot{\varepsilon}_{ij}^{pl}\dot{\varepsilon}_{ij}^{pl}\right)^{\frac{1}{2}} \tag{17}$$

where $\dot{\varepsilon}_{ij}^{pl}$ denotes the plastic strain tensor.

Therefore, the isotropic hardening relationship between the isotropic stress and cumulative plastic strain reads

$$R = R_{\infty}(1 - exp(-h \times p)) \tag{18}$$

where h refers to the rate at which the size of the yield surface changes as the plastic strain develops.

R_{∞} represents the maximum expansion of the yield surface.

The nonlinear kinematic hardening relationship between the incremental backstress tensor and cumulative plastic strain rate $\dot{p}$ reads

$$dX_{ij} = \frac{2}{3}C\dot{\varepsilon}_{\mathrm{ij}}^{\mathrm{pl}} - \gamma \times X_{ij}\dot{p} \tag{19}$$

This study follows the calibration procedure in ABAQUS (2014) based on the experimental low-cycle fatigue test. For isotropic hardening parameters, the experimental cycles can be interpreted approximately as repeated cycles over the same plastic strain range $\Delta\varepsilon^{pl}$. The size of the yield surface σ_y^i in the ith cycle thus follows

$$\sigma_y^i = \frac{\sigma_i^t - \sigma_i^c}{2} \tag{20}$$

where σ_y^i, σ_i^t and σ_i^c denote the size of the yield surface, the peak tensile stress and the yielding compressive stress at the ith cycle, respectively. The effective, cumulative plastic strain p_i at the ith cycle is

$$p_i = \frac{1}{2}(4i - 3)\Delta\varepsilon_o^{pl} \tag{21a}$$

$$\Delta\varepsilon_o^{pl} = \Delta\varepsilon - 2\frac{\sigma_1^t}{E} \tag{21b}$$

where $\Delta\varepsilon$ denotes the strain range and σ_1^t represents the tensile peak stress at the first cycle.

For the kinematic hardening parameters, this study adopts two nonlinear kinematic hardening expressions by Chaboch (1986, 1989). Based on the stabilized cycle in the low-cycle fatigue test, the backstress derives from the integration of the backstress evolution laws over the uniaxial strain cycle, with an exact match for the first data pair $(\sigma_1, 0)$

$$X_1 = \frac{C_1}{\gamma_1}(1 - e^{-\gamma_1 p}) + X_1^o \times e^{-\gamma_1 p} \tag{22a}$$

$$X_2 = \frac{C_2}{\gamma_2}(1 - e^{-\gamma_2 \times p}) + X_2^o \times e^{-\gamma_2 \times p} \tag{22b}$$

where X_1^o and X_2^o denote the first and second backstress at the first point, which is the initial value of the backstress. After shifting the strain axis to p_0, the data pair $(\sigma_i, \varepsilon_i^p)$ in the saturated cycle follows

$$\alpha_i = \sigma_i - \frac{\sigma_1 + \sigma_n}{2} \tag{23a}$$

$$p_i = \varepsilon_i - \frac{\sigma_i}{E} - \varepsilon_p^o \tag{23b}$$

where $p_1 = 0$ and p_0 refer to the strain value at the intersections between the stress-strain curve and the horizontal strain axis.

4.3 Identification of damage variables

The damage in CDM characterizes the effective surface density of microcracks in a Representative Volume Element (RVE). The cumulative plastic strain triggers the microstructural dislocations, nucleation of microscopic flaws and growth of the microscopic flaws into microcracks. Damage initiates when the local strain energy driving the fatigue failure exceeds the threshold stored energy required to incubate the defects (Lemaitre and Desmorat 2005). Therefore, the threshold stored energy quantifies the damage initiation. However, measurement of the threshold stored energy remains experimentally challenging. According to the dissipation state potential theory, Lemaitre (2012) defines the relationship between the stored energy with the cumulative plastic strain

$$\begin{aligned} w^s &= \int_0^t \left(R\dot{r} + X_{ij}\dot{\alpha}_{ij}\right)dt \\ &\approx R_{\infty}p + \frac{3}{4C}X_{ij}X_{ij} \qquad \text{if } D = 0 \end{aligned} \tag{24}$$

Based on Eq. (24), the threshold stored energy value w_D^s corresponds to the threshold cumulative plastic strain p_D. Experimental evidences (Lemaitre 2012, Lemaitre and Desmorat 2005) illustrate that the threshold of the stored energy value remains constant for different loading types. Based on Eq. (24), the threshold cumulative plastic strain thus is also a constant. However, this constant value contradicts the experimental measurement (see following discussion on Fig. 13). Therefore, a new damage initiation criterion, which is easy to measure experimentally, becomes necessary.

Based on the continuum damage mechanics, the variation of the stress amplitude under low-cycle fatigue consists of two phases as shown in Fig. 13(a): (1) the material stabilization phase with zero damage; and (2) the decrease in the stress amplitude caused by the increasing damage variable. The damage therefore quantifies the variation in the stress amplitude in the second phase (Lemaitre 2012)

$$D = 1 - \frac{\sigma_a}{{\sigma^*}_a} \tag{25}$$

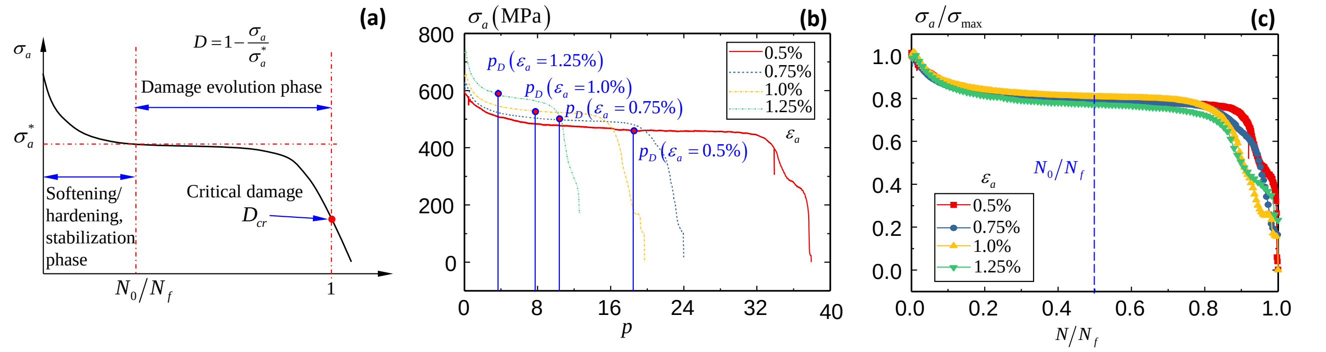

Fig. 13 (a) Schematic variation of the stress amplitude with normalized fatigue cycles; (b) variation of the stress amplitude with cumulative plastic strain; (c) variation of the stress amplitude with normalized fatigue cycles

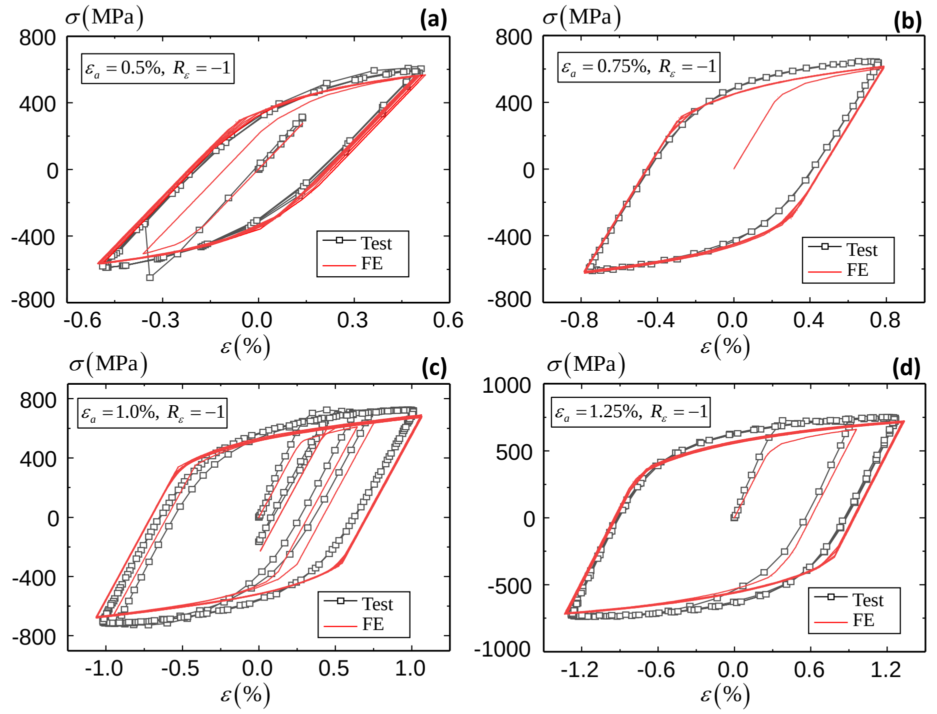

Fig. 14 Comparison of the stress-strain curves from experimental tests and numerical simulations

where σ_a^* represents the stress amplitude at the end of stabilization phase and σ_a denotes the stress amplitude. Therefore, this study defines the damage initiation at the inflection point in σ_a N/N_f curve (see Fig. 13(a)). According to Eq. (25), Fig. 13(b) indicates a strong variation of the threshold cumulative plastic strain p_D among different applied strain amplitudes, contrary to the initial assumption that damage initiates at a constant threshold p_D value under different loadings in the Lemaitre's model (Lemaitre 2012). This study, therefore, proposes a damage initiation criterion based on the fraction of the total fatigue life after reviewing different steel materials under low-cycle loadings (Branco *et al.* 2012, Paul *et al.* 2015, Feng and Qian 2018, Veerababu *et al.* 2017, Guo *et al.* 2013, Okamura *et al.* 1999, Sarkar *et al.* 2015, Roy *et al.* 2012, Gao *et al.* 2019). Fig. 13(c) demonstrates that the initiation $\frac{N_0}{N_f}$ ratio remains approximately constant (at about 0.5) corresponding to the damage defined in Eq. (25). Other researchers have reported a similar observation (Feng and Qian 2018, Guo *et al.* 2013, Hu *et al.* 2013, Okamura *et al.* 1999).

4.4 Rapid estimation of S-N curve

Based on continuum damage mechanics, this section introduces a hybrid approach (see Appendix) to determine the low-cycle fatigue life based on only one fatigue test and one monotonic tensile test.

4.4.1 Calibration of the elastic-plastic material parameters

According to the procedure in section 4.2, this study calibrates the isotropic hardening parameters by fitting Eqs. (20) and (21) and the kinematic hardening parameters by fitting Eqs. (22) and (23). Table 4 shows the calibrated

Table 4 Parameters in the combined isotropic/kinematic hardening model at –60°C

ε_a	E(MPa)	σ_y^o(MPa)	Q_∞(MPa)	h	C_1(MPa)	γ_1	C_2(MPa)	γ_2
0.5%	198503	421	-55	0.34	29140	66	83613	991
0.75%	188045	461	-63	0.84	21311	78	39922	616
1.0%	189464	509	-72	0.8	15977	32	32172	485
1.25%	184484	525	-85	0.87	18982	76	23000	517

cyclic plastic material properties under different strain amplitudes. Fig. 14 illustrates a good agreement in the stress-strain curve measured in the experiment and those from the numerical simulation based on properties in Table 4.

4.4.2 Definition of S-N relationship based on CDM

Based on the potential function of the damage F_D in Eq. (16), the damage evolution under the uniaxial low-cycle fatigue reads

$$\dot{D} = \frac{\partial F_D}{\partial Y}\dot{\lambda} = \left(\frac{\sigma^2}{2ES(1-D)^2}\right)^s \dot{p} \tag{26a}$$

$$(1-D)^{2s}\dot{D} = \left(\frac{\sigma^2}{2ES}\right)^s \dot{p} = \frac{\sigma^{2s}\times\dot{p}}{(2ES)^s} \tag{26b}$$

With the assumption that the damage is constant in each cycle, Eq. (26) thus represents the damage accumulation in a cycle. Lemaitre’s model (Lemaitre 2012, Lemaitre and Desmorat 2005), assumes a simplified, perfectly plastic material in each cycle, which does not correspond to the experimental results. Therefore, this study rewrites Eq. (26) as

$$(1-D)^{2s}dD = \frac{\sigma^{2s}dp}{(2ES)^s} = \frac{W_N^{2s}}{(2ES)^s}dN \tag{27}$$

where W_N^{2s} at N*th* cycle follows

$$W_N^{2s} = \int_{Nth\ cycle} \sigma^{2s}dp \tag{28}$$

After normalizing the W_N^{2s} by the initial value of W_1^{2s}

$$W_N^{2s} = W_1^{2s}\times f_{2s}\left(\frac{N}{N_f}\right) \tag{29}$$

where $f_{2s}(N/N_f)$ is the ratio of $\frac{W_N^{2s}}{W_1^{2s}}$. The function $f_{2s}(N/N_f)$ describes a similar variation of the normalized stress amplitude (Fig. 3(b)), which shows the same function for different strain amplitudes. Therefore, Eq. (27) becomes

$$(1-D)^{2s}dD = \frac{N_f\times W_1^{2s}}{(2ES)^s}\times f_{2s}\left(\frac{N}{N_f}\right)d\frac{N}{N_f} \tag{30a}$$

Integrating both sides of Eq. (30a) leads to

$$\int_0^{D_{cr}}(1-D)^{2s}dD = \frac{N_f\times W_1^{2s}}{(2ES)^s}\times\int_{\frac{N_0}{N_f}}^1 f_{2s}\left(\frac{N}{N_f}\right)d\frac{N}{N_f} \tag{30b}$$

where D_{cr} denotes the critical damage at the end of the fatigue life. Replacing the integrals in Eq. (30b) by two discrete functions, we have

$$F_D^{2s}(D_{cr}) = \frac{N_f\times W_1^{2s}}{(2ES)^s}\times F_{2s} \tag{31a}$$

$$N_f\times W_1^{2s} = \frac{F_D^{2s}(D_{cr})\times(2ES)^s}{F_{2s}} = U \tag{31b}$$

where the new fatigue indicator W_1^{2s} refers to the integral in Eq. (28) in the first cycle.

4.4.3 Calibration of damage parameters

To calibrate the damage parameters, Eq. (31) alone is insufficient for solving the two material parameters *S* and *s*. However, based on the thermodynamic continuum damage mechanics, *S* and *s* depend solely on the temperature (Lemaitre 2012, Lemaitre and Desmorat 2005). Therefore, the damage evolution in a monotonic tension test provides another convenient equation. The damage in monotonic tensile tests also defines the drop in true stress from the ultimate strength. For the monotonic tensile, the plasticity criterion follows

$$f = \frac{\sigma}{1-D} - \sigma_u = 0 \tag{32}$$

where σ_u denotes the ultimate strength. Therefore, the energy density release rate Y for the axial monotonic tests follows

$$Y = \frac{\sigma_u^2}{2E} \tag{33}$$

Based on the unified damage evolution law, the energy density release rate Y for the axial monotonic tests follows

$$\dot{D} = \left(\frac{Y}{S}\right)^s\dot{p} = \left(\frac{\sigma_u^2}{2ES}\right)|\dot{\varepsilon}_p| \tag{34}$$

Therefore, after a simple integration, the critical value of damage derives from

$$D_{cr} = \left(\frac{{\sigma_u}^2}{2ES}\right)^s(\varepsilon_{pR}^* - \varepsilon_{pD}) \tag{35}$$

where ε_{pR}^* defines the local rupture strain in the necking zone and ε_{pD} represents the damage threshold of plastic strain when the damage initiates. The values of the ε_{pR}^* and ε_{pD} correspond to

$$\varepsilon_{pD} = \varepsilon_p(\sigma = \sigma_u) \tag{36a}$$

$$\varepsilon_{pR}^* = 2\left(1 - \sqrt{1 - Z}\right) \tag{36b}$$

$$Z = \frac{(S_0 - S_R)}{S_0} \tag{36c}$$

where S_0 and S_R are the area of cross-section in the initial intact specimen and at the necking location, as shown in Fig. 15(a).

$$D_{cr} = 1 - \frac{\sigma_R}{\sigma_u} \tag{37}$$

where σ_R is rupture strength under monotonic tension. Therefore, combining Eqs. (31) and (35) allows solving for the parameters *s* and *S*.

4.4.4 Verification for S550 under the low temperature

To solve the above damage related parameters *s* and *S*, this study conducted a monotonic tension test at –60°C. Fig. 15(a) shows the monotonic stress-strain curve at –60°C. Based on the monotonic tension test result, the critical damage variables are: $D_{cr} = 0.49$, $\varepsilon_{pD} = 0.09$, $\sigma_u = 783$ MPa. According to the rupture failure surface, we have $S_0 = 12.5 \times 22\ \mathrm{mm}^2$, $S_R = 8 \times 18\ \mathrm{mm}^2$, $Z = 0.476$ and $\varepsilon_{pR}^* = 0.553$.

Based on the low-cycle fatigue test with the strain ratio of 0.75%, the damage initiates at the $\frac{N_0}{N_f}$ of 0.5 (based on the damage initiation definition in Section 4.3). The normalized function of $f_{2s}(N/N_f)$ can be approximated using polynomials for different *s* values as shown in Fig. 15(b). The solutions of *s* and *S* correspond to the intersection between the *S*-*s* curves for the cyclic loading

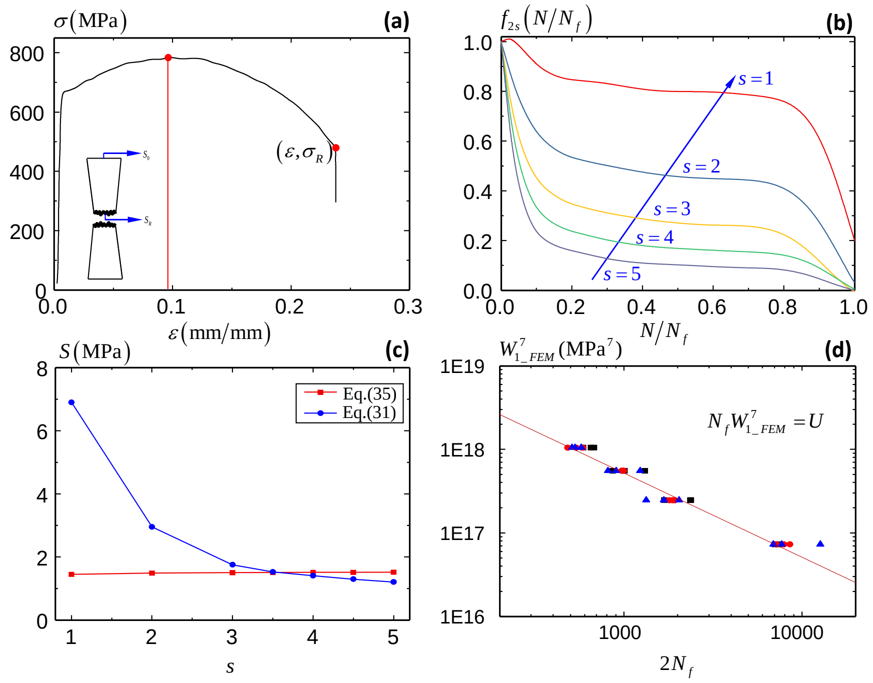

Fig. 15 (a) Monotonic stress strain curve of S550 at –60°C; (b) variation of the $f_{2s}(N/N_f)$ with different *s* values; (c) determination of *S* and *s* values; (d) assessment of low-cycle fatigue tests based on W_1^7(FEM) and Eq. (38)

Table 5 Comparison between the experimental fatigue life and predicted fatigue life by Eq. (35)

ε_a	0.5%	0.75%	1.0%	1.25%
W_1^7 (FEM)	7.31×10^{16}	2.47×10^{17}	5.54×10^{17}	1.05×10^{18}
$\tilde{N}_f$ (test) (test)(experimental)	3612	1068	530	319
$\tilde{N}_f[Eq.(38)]$	2453	1068	476	252
$\frac{\tilde{N}_f(test)}{\tilde{N}_f[Eq.(38)]}$ (test)	1.47371	1	1.11345	1.26587
Mean	1.21			
CoV	0.36			

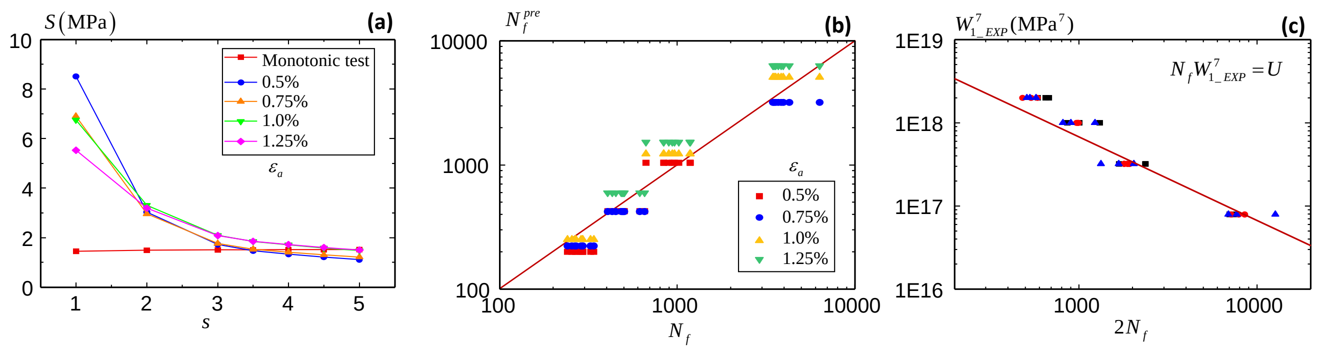

Fig. 16 (a) S and s solutions for different strain ratios; (b) comparison between the measured and predicted fatigue life; (c) assessment of low-cycle fatigue data based on $W_{1\_EXP}^7$ and Eq. (38)

(Eq. (31)) and the monotonic loading (Eq. (35)), and are 3.5 and 1.50 MPa, as shown in Fig. 15(c).

Based on the calibrated elastic-plastic material parameters under the strain amplitude of 0.75% in Table 4, the numerical simulation of the coupon specimen by ABAQUS (2014) helps to calculate the corresponding value of W_1^{2s} under different strain amplitudes. Therefore, the corresponding fatigue life under different strain amplitudes follows

$$N_f W_1^7 = U \tag{38}$$

Table 5 lists the numerically calculated W_1^7 and the corresponding fatigue life based on Eq. (38) for the strain ratio of –1. Due to the negligible mean stress effect, Fig. 15(d) compares the experimental test results with the S-N curve (Eq. (38)) based on the numerically calculated W_1^7. The good agreement between the predicted fatigue life and experimental fatigue life proves the effectiveness of the proposed hybrid approach.

5. Discussion

The above section introduces the framework of continuum damage mechanics and a hybrid approach to rapidly estimate the S-N curve based on one set of fatigue tests and one set of monotonic tension tests. This section discusses the sensitivity of the damage parameters with respect to the choice of the fatigue test.

An important assumption adopted in this paper is the material's similarity under the uniaxial low-cycle fatigue loadings. A similar trend of the stress or the energy indicator variation with increasing normalized fatigue cycles under different strain amplitudes is essential for this hybrid approach. The material similarity refrains from complex iterations to determine the damage evolution, which is reasonable and prevalent for various steels (Paul *et al*. 2015, Feng and Qian 2018, Veerababu *et al*. 2017, Sarkar *et al*. 2015).

The above verification of the hybrid approach in Section 4.4.4 is based on the low-cycle fatigue test under the strain amplitude of 0.75%. This study also calculates the corresponding values of s and S based on other three low-cycle fatigue tests with the strain amplitudes of 0.5%, 1.0% and 1.25%. Fig. 16(a) compares S-s curve at different cyclic loading levels with the monotonic tensile test. The intersection between the monotonic and cyclic S-s curve represents the S-s solutions for different strain amplitudes. Fig. 16(b) compares the predicted fatigue life with the actual experimental fatigue life based on the fatigue test under different strain amplitudes. A reasonable agreement between them verifies the robustness of the proposed hybrid approach. This study also estimates the fatigue life based on experimental value of $W_{1\_EXP}^7$ under the strain amplitude of 0.75%. As illustrated in Fig.16c, the S-N curve based on the experimental value of $W_{1\_EXP}^7$ provides a conservative assessment under the larger strain amplitude, with a reasonable agreement.

6. Conclusions

This study presents experimental results of low-cycle fatigue tests on S550 high-strength steel at –60°C with three different strain ratios of –1, 0.1 and 0.5. To alleviate the time-consuming and expensive fatigue tests, this paper proposes an energy-based fatigue driving force and a hybrid approach to rapidly determine the S-N curve based on continuum damage mechanics. The above investigations in this study support the following conclusions.

- At –60°C, the variation of the normalized stress amplitude shows a similar trend with the normalized fatigue cycles for different strain amplitudes. The S550 steel at –60°C shows a non-Masing type behavior. The fatigue failure surface includes three regions: the crack initiation zone, the crack propagation zone, and the slant fracture zone. The crack initiation originates from the internal defects and the reversed slip band. In contrast to the dominant striations on the fatigue crack growth surface at the room temperature, the crack growth surface at –60°C shows clear cleavage features. In the final fracture zone, the granular and rough fracture surfaces with clear macroscopic fatigue marks emerge.
- The initial non-zero mean stress for different strain ratios dissipates to a zero value within 10% of the fatigue life. Due to the quick mean stress relaxation

for S550, the effect due to different strain ratios on the total low-cycle fatigue life becomes negligible.

- Under the same strain amplitude, the low temperature slightly shortens the fatigue life under the strain ratios of 0.1 and 0.5. The decrease in the fatigue life correspond to a larger dissipated energy enclosed in the hysteresis loop at the low temperature. Therefore, the energy indicator can better integrate the assessment of the low-cycle fatigue life under different temperatures.
- After examining the damage initiation criterion in various steels, this study proposes a new initiation criterion based on the fraction of the total fatigue life. Thereafter, a new S-N relationship based on the physical fatigue indicator W_1^{2s} derives from the continuum damage mechanics. This new S-N relationship relies on a hybrid approach, which combines one set of fatigue tests and one set of monotonic tensile tests to determine the two material parameters (s and S). The experimental tests in this paper validates the hybrid approach

Acknowledgments

The authors thank the National Research Foundation, Keppel Corporation and National University of Singapore for supporting this work done in the Keppel-NUS Corporate Laboratory. The conclusions put forward reflect the views of the authors alone, and not necessarily those of the institutions within the Corporate Laboratory. The President Graduate Fellowship to the first author provided by the National University of Singapore, are highly acknowledged.

References

ABAQUS (2014), Abaqus Analysis User's Guide. Version 6.14. Providence, RI, USA. Version 6.14, Dassault Systèmes Simulia Corp.

ABS (2014), Fatigue assessment of offshore structures, American Bureau of Shipping.

Aeran, A., Siriwardane, S.C., Mikkelsen, O. and Langen, I. (2017), "A new nonlinear fatigue damage model based only on SN curve parameters", *Int. J. Fatigue*, **103**, 327-341. https://doi.org/10.1016/j.ijfatigue.2017.06.017

Amiri, M. and Khonsari, M. (2010), "Rapid determination of fatigue failure based on temperature evolution: Fully reversed bending load", *Int. J. Fatigue*, **32**, 382-389. https://doi.org/10.1016/j.ijfatigue.2009.07.015

Arcari, A., De Vita, R. and Dowling, N.E. (2009), "Mean stress relaxation during cyclic straining of high strength aluminum alloys", *Int. J. Fatigue*, **31**, 1742-1750. https://doi.org/10.1016/j.ijfatigue.2009.01.021

ASTM (2012), E606/E606M−12. Standard Test Method for Strain-Controlled Fatigue Testing, ASTM International, West Conshohocken, PA, USA.

Bonora, N. and Newaz, G. (1998), "Low cycle fatigue life estimation for ductile metals using a nonlinear continuum damage mechanics model", *Int. J. Solids Struct.*, **35**, 1881-1894. https://doi.org/10.1016/S0020-7683(97)00139-X

Botshekan, M., Degallaix, S., Desplanques, Y. and Pol, J. (1998), "Tensile and LCF properties of AISI 316LN SS at 300 and 77 K.", *Fatigue Fract. Eng. Mater. Struct.*, **21**, 651-660. https://doi.org/10.1046/j.1460-2695.1998.00058.x

Branco, R., Costa, J. and Antunes, F. (2012), "Low-cycle fatigue behaviour of 34CrNiMo6 high strength steel", *Theor. Appl. Fract. Mech.*, **58**, 28-34. https://doi.org/10.1016/j.tafmec.2012.02.004

Chaboche, J.-L. (1986), "Time-independent constitutive theories for cyclic plasticity", *Int. J. Plast.*, **2**, 149-188. https://doi.org/10.1016/0749-6419(86)90010-0

Chaboche, J.-L. (1989), "Constitutive equations for cyclic plasticity and cyclic viscoplasticity", *Int. J. Plast.*, **5**, 247-302. https://doi.org/10.1016/0749-6419(89)90015-6

Chaboche, J. and Lesne, P. (1988), "A non-linear continuous fatigue damage model", *Fatigue Fract. Eng. Mater. Struct.*, **11**, 1-17. https://doi.org/10.1111/j.1460-2695.1988.tb01216.x

Chen, S., Qian, X. and Ahmed, A. (2016), "Cleavage fracture assessment for surface-cracked plate fabricated from high strength steels", *Eng. Fract. Mech.*, **161**, 1-20. https://doi.org/10.1016/j.engfracmech.2016.04.039

Darveaux, R. (2002), "Effect of simulation methodology on solder joint crack growth correlation and fatigue life prediction", *J. Electron. Packag.*, **124**, 147-154. https://doi.org/10.1109/ECTC.2000.853299

Ellyin, F. (1989), Cyclic strain energy density as a criterion for multiaxial fatigue failure, *Biaxial and Multiaxial Fatigue*, (Edited by M.W. Brown and K.J. Miller), Mechanical Engineering Publications, London, UK, pp. 571-583.

Ertas, A.H. and Yilmaz, A.F. (2014), "Simulation-based fatigue life assessment of a mercantile vessel", *Struct. Eng. Mech., Int. J.*, **50**(6), 835-852. https://doi.org/10.12989/sem.2014.50.6.835

Feng, L. and Qian, X. (2017), "A hot-spot energy indicator for welded plate connections under cyclic axial loading and bending", *Eng. Struct.*, **147**, 598-612. https://doi.org/10.1016/j.engstruct.2017.06.021

Feng, L. and Qian, X. (2018), "Low cycle fatigue test and enhanced lifetime estimation of high-strength steel S550 under different strain ratios", *Mar. Struct.*, **61**, 343-360. https://doi.org/10.1016/j.marstruc.2018.06.011

Frederick, C.O. and Armstrong, P. (1966), A mathematical representation of the multiaxial Bauschinger effect, CEGB Report, RD/B/n731.

Gao, C., Ren, T. and Liu, M. (2019), "Low-cycle fatigue characteristics of Cr18Mn18N0. 6 austenitic steel under strain controlled condition at 100°C", *Int. J. Fatigue*, **118**, 35-43. https://doi.org/10.1016/j.ijfatigue.2018.08.038

Ghazijahani, T.G., Jiaoa, H. and Hollowayb, D. (2015), "Fatigue tests of damaged tubes under flexural loading", *Steel Compos. Struct., Int. J.*, **19**(1), 223-236. https://doi.org/10.12989/scs.2015.19.1.223

Gróza, M. and Váradi, K. (2017), "Total fatigue life analysis of a nodular cast iron plate specimen with a center notch", *Adv. Mech. Eng.*, **9**(12), 1-11. https://doi.org/10.1177/1687814017742546

Guo, P., Qian, L., Meng, J., Zhang, F. and Li, L. (2013), "Low-cycle fatigue behavior of a high manganese austenitic twin-induced plasticity steel", *Mater. Sci. Engi. A- Struct. Mater.*, **584**, 133-142. https://doi.org/10.1016/j.msea.2013.07.020

Hobbacher, A. (2016), *Recommendations for fatigue design of welded joints and components*, (2nd Edition), International Institute of Welding, Springer.

Hu, X., Huang, L., Wang, W., Yang, Z., Sha, W., Wang, W., Yan, W. and Shan, Y. (2013), "Low cycle fatigue properties of CLAM steel at room temperature", *Fusion. Eng. Des.*, **88**, 3050-3059. https://doi.org/10.1016/j.fusengdes.2013.08.001

Huang, Z., Wang, O., Wagner, D. and Bathias, C. (2014), "Constitutive model coupled with damage for carbon manganese steel in low cycle fatigue", *Steel Compos. Struct., Int. J.*, **17**(2), 185-198. https://doi.org/10.12989/scs.2014.17.2.185

Ju, X., Zeng, Z., Zhao, X. and Liu, X. (2018), "Fatigue study on additional cutout between U shaped rib and floorbeam in orthotropic bridge deck", *Steel Compos. Struct., Int. J.*, **28**(3), 319-329. https://doi.org/10.12989/scs.2018.28.3.319

Kawasaki, T., Nakanishi, S., Sawaki, Y., Hatanaka, K. and Yokobori, T. (1975), "Fracture toughness and fatigue crack propagation in high strength steel from room temperature to −180°C", *Eng. Fract. Mech.*, **7**(3), 465-472. https://doi.org/10.1016/0013-7944(75)90047-8

Koh, S. and Stephens, R. (1991), "Mean stress effects on low cycle fatigue for a high strength steel", *Fatigue Fract. Eng. Mater. Struct.*, **14**, 413-428. https://doi.org/10.1111/j.1460-2695.1991.tb00672.x

Kourousis, K.I. and Dafalias, Y.F. (2013), "Constitutive modeling of Aluminum Alloy 7050 cyclic mean stress relaxation and ratcheting", *Mech. Res. Commun.*, **53**, 53-56. https://doi.org/10.1016/j.mechrescom.2013.08.001

Lau, J.H., Pan, S.H. and Chang, C. (2002), "A new thermal-fatigue life prediction model for wafer level chip scale package (WLCSP) solder joints", *J. Electron. Packag.*, **124**, 212-220. https://doi.org/10.1115/1.1462625

Lee, C.-H., Van Do, V.N. and Chang, K.-H. (2014), "Analysis of uniaxial ratcheting behavior and cyclic mean stress relaxation of a duplex stainless steel", *Int. J. Plast*., **62**, 17-33. https://doi.org/10.1016/j.ijplas.2014.06.008

Lefebvre, D. and Ellyin, F. (1984), "Cyclic response and inelastic strain energy in low cycle fatigue", *Int. J. Fatigue*, **6**, 9-15. https://doi.org/10.1016/0142-1123(84)90003-3

Lemaitre, J. (2012), *A course on damage mechanics*, Springer Science & Business Media.

Lemaitre, J. and Desmorat, R. (2005), *Engineering damage mechanics: ductile, creep, fatigue and brittle failures*, Springer Science & Business Media.

Liao, X., Wang, Y., Qian, X. and Shi, Y. (2018), "Fatigue crack propagation for Q345qD bridge steel and its butt welds at low temperatures", *Fatigue Fract. Eng. Mater. Struct.*, **41**(3), 675-687. https://doi.org/10.1111/ffe.12727

Lim, C., Choi, W. and Sumner, E.A. (2013), "Parametric study using finite element simulation for low cycle fatigue behavior of end plate moment connection", *Steel Compos. Struct*., *Int. J*., **14**(1), 57-71. https://doi.org/10.12989/scs.2013.14.1.057

Liu, Y., Xiong, Z., Feng, Y. and Jiang, L. (2017), "Concrete-filled rectangular hollow section X joint with Perfobond Leister rib structural performance study: Ultimate and fatigue experimental Investigation", *Steel Compos. Struct., Int. J.*, **24**(4), 455-465. https://doi.org/10.12989/scs.2017.24.4.455

Maachou, S., Boulenouar, A., Benguediab, M., Mazari, M. and Ranganathan, N. (2016), "Plastic energy approach prediction of fatigue crack growth", *Struct. Eng. Mech., Int. J.*, **59**(5), 885-899. https://doi.org/10.12989/sem.2016.59.5.885

Maalek, S., Heidary-Torkamani, H., Pirooz, M.D. and Naeeini, S.T.O. (2019), "Numerical investigation of cyclic performance of frames equipped with tube-in-tube buckling restrained braces", *Steel Compos. Struct., Int. J.*, **30**(3), 201-215. https://doi.org/10.12989/scs.2019.30.3.201

Macha, E. and Sonsino, C. (1999), "Energy criteria of multiaxial fatigue failure", *Fatigue. Fract. Eng. Mater. Struct.*, **22**, 1053-1070.

Malagi, R.R. and Danawade, B.A. (2015), "Fatigue behavior of circular hollow tube and wood filled circular hollow steel tube", *Steel. Compos. Struct., Int. J.*, **19**(3), 585-599. https://doi.org/10.12989/scs.2015.19.3.585

Okamura, H., Ohtani, R., Saito, K., Kimura, K., Ishii, R., Fujiyama, K., Hongo, S., Iseki, T. and Uchida, H. (1999), "Basic investigation for life assessment technology of modified 9Cr–1Mo steel", *Nucl. Eng. Des.*, **193**, 243-254. https://doi.org/10.1016/S0029-5493(99)00181-8

Paul, S.K., Stanford, N., Taylor, A. and Hilditch, T. (2015), "The effect of low cycle fatigue, ratcheting and mean stress relaxation on stress–strain response and microstructural development in a dual phase steel", *Int. J. Fatigue*, **80**, 341-348. https://doi.org/10.1016/j.ijfatigue.2015.06.003

Perera, R., Gomez, S. and Alarcon, E. (2001), "Seismic assessment of steel structures through a cumulative damage", *Steel. Compos. Struct., Int. J.*, **1**(3), 283-294. https://doi.org/10.12989/scs.2001.1.3.283

Roy, S.C., Goyal, S., Sandhya, R. and Ray, S. (2012), "Low cycle fatigue life prediction of 316 L (N) stainless steel based on cyclic elasto-plastic response", *Nucl. Eng. Des.*, **253**, 219-225. https://doi.org/10.1016/j.nucengdes.2012.08.024

Sakr, M.A., Eladly, M.M., Khalifa, T. and El-Khoriby, S. (2019), "Cyclic behaviour of infilled steel frames with different beam-to-column connection types", *Steel Compos. Struct., Int. J.*, **30**(5), 443-456. https://doi.org/10.12989/scs.2019.30.5.443

Sarkar, A., Kumawat, B.K. and Chakravartty, J. (2015), "Low cycle fatigue behavior of a ferritic reactor pressure vessel steel", *J. Nucl. Mater.*, **462**, 273-279. https://doi.org/10.1016/j.jnucmat.2015.04.015

Shang, D.-G. and Yao, W.-X. (1999), "A nonlinear damage cumulative model for uniaxial fatigue", *Int. J. Fatigue*, **21**, 187-194. https://doi.org/10.1016/S0142-1123(98)00069-3

Shibata, K., Kishimoto, Y., Namura, N. and Fujita, T. (1985), "Cyclic softening and hardening of austenitic steels at low temperatures", *Fatigue Low Temperat*. https://doi.org/10.1520/STP32745S

Veerababu, J., Goyal, S., Sandhya, R. and Laha, K. (2017), "Low cycle fatigue behaviour of Grade 92 steel weld joints", *Int. J. Fatigue*, **105**, 60-70. https://doi.org/10.1016/j.ijfatigue.2017.08.013

Veritas, D.N. (2010), *Fatigue design of offshore steel structures*, DNV Recommended Practice DNV-RP-C203.

Walters, C.L., Alvaro, A. and Maljaars, J. (2016), "The effect of low temperatures on the fatigue crack growth of S460 structural steel", *Int. J. Fatigue*, **82**, 110-118. https://doi.org/10.1016/j.ijfatigue.2015.03.007

Wang, M., Shi, Y., Wang, Y., Xiong, J. and Chen, H. (2013), "Degradation and damage behaviors of steel frame welded connections", *Steel Compos. Struct., Int. J.*, **15**(4), 357-377. https://doi.org/10.12989/scs.2013.15.4.357

Ye, D. and Wang, Z. (2001), "A new approach to low-cycle fatigue damage based on exhaustion of static toughness and dissipation of cyclic plastic strain energy during fatigue", *Int. J. Fatigue*, **23**, 679-687. https://doi.org/10.1016/S0142-1123(01)00027-5

Zhang, Z. and Qian, X. (2016), "A local approach to estimate cleavage angles in steel under mixed-mode I and II conditions", *Eng. Fract. Mech.*, **166**, 164-181. https://doi.org/10.1016/j.engfracmech.2016.08.024

Zhang, L., Liu, X., Wu, S., Ma, Z. and Fang, H. (2013), "Rapid determination of fatigue life based on temperature evolution", *Int. J. Fatigue*, **54**, 1-6. https://doi.org/10.1016/j.ijfatigue.2013.04.002

Zhao, X., Tian, Y., Jia, L.-J. and Zhang, T. (2018), "Ultra-low cycle fatigue tests of Class 1 H-shaped steel beams under cyclic pure bending", *Steel Compos. Struct., Int. J.*, **26**(4), 439-452. https://doi.org/10.12989/scs.2018.26.4.439

BU

Appendix: Hybrid approach combining fatigue and monotonic tests

Fig. A1 summarizes the hybrid approach, which compromises of three steps:

Step 1. Conduct the monotonic tension tests (with three duplicated specimens) to measure the static material properties including the critical damage value D_{cr}. Conduct the fatigue test (with minimum three duplicated specimens) to measure the cyclic material properties.

Step 2. Calibrate the elastic-plastic material parameters following the procedure in Section 4.2 and determine the ratio of the fatigue damage initiation over the total fatigue life based on the stress variation with normalized fatigue cycles. Fit the variation of $f_{2s}\left(\frac{N}{N_f}\right)$ using polynomial functions for different *s* values.

Step 3. Determine the two material damage parameters *S* and *s* from Eq. (35) of the monotonic tensile test and Eq. (31) of the low-cycle fatigue test, based on the parameters obtained in Step 1 and 2. Compute the fatigue indicator W_1^{2s} to predict the corresponding fatigue life based on Eq. (38).

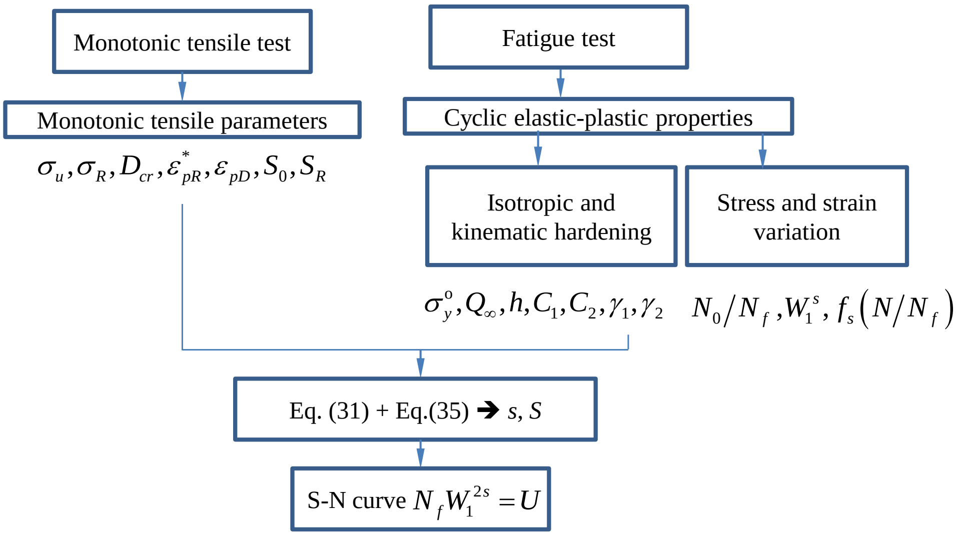

Fig. A1 Flow chart of the hybrid approach